TECHNICAL INNOVATION

Non-invasive mapping of interstitial fluid pressure in microscale tissues

Ozgur Ozsun,[ab] Rebecca L. Thompson,[c] Kamil L. Ekinci†*[abd] and Joe Tien‡*[cd]

This study describes a non-invasive method for mapping interstitial fluid pressure within hydrogel-based microscale tissues. The method is based on embedding (or forming) a tissue within a silicone (PDMS) microfluidic device, and measuring the extremely slight displacement (<1 μm) of the PDMS optically when the device is pressurized under static and flow conditions. The displacement field under uniform pressure provides a map of the local device stiffness, which can then be used to obtain the non-uniform pressure field under flow conditions. We have validated this method numerically and applied it towards determining the hydraulic properties of tumor cell aggregates, blind-ended epithelial tubes, and perfused endothelial tubes that were all cultured within micropatterned collagen gels. The method provides an accessible tool for generating high-resolution maps of interstitial fluid pressure for studies in mechanobiology.

Insight, innovation, integration

Interstitial fluid pressure (IFP) is believed to influence cell behavior in both normal and pathological states. Direct testing of this hypothesis *in vitro* has been limited by current, relatively crude methods to estimate IFP. This study provides an *innovative* non-invasive optical technique to map IFP in microscale tissues with high spatial and temporal resolution. When applied to tumor cell aggregates, epithelial tubes, or perfused endothelial vessels that are cultured under pressure gradients, this technique yields *insights* into the hydraulic properties of these tissues and how they may vary with IFP. This technique thus enables the *integration* of IFP towards a more complete understanding of the interplay between physical signals and cell function.

Introduction

Flows through extracellular matrices and other porous media are common in biological processes and are driven by gradients in interstitial fluid pressure (IFP).[1] As a component of the physical microenvironment, IFP can affect cell behavior by controlling the distribution of local stresses and chemical gradients.[2,3] These effects have been particularly well-studied in the context of elevated IFP that accompanies tumor progression *in vivo*.[4] Many groups are interested in using engineered tissues to study the effects of IFP on biological processes, such as tumor cell invasion and angiogenesis, in a more controlled

environment *in vitro*.[5–7] These *in vitro* experiments typically culture cells in a gel within a silicone (PDMS) microfluidic device, interface the sides of the gel to known pressures, and correlate the resulting cell behavior with the interstitial environment. To realize the potential of this approach, it is important to be able to measure IFP accurately and with high spatial resolution.

Currently, nearly all of the techniques that can measure IFP are invasive, in that they rely on interfacing the porous material with an external element (*e.g.,* liquid column, air bubble, or wick-containing needle).[8–10] While such techniques do allow for precise measurement of local IFP, they require relatively large volumes of liquid to be transferred through the porous material before changes in a pressure transducer (*e.g.,* in the height of a water column) are observable. Since tissues and gels are hydraulically resistive, application of these invasive techniques to such materials may result in low temporal resolution and flow-induced alterations of IFP. A non-invasive technique to measure IFP would allow the porous material to exist in its native state without potentially confounding effects due to fluid flow to, from, or around a discrete measurement port.

Here, we describe a technique to map IFP in microscale tissues that are formed within PDMS microfluidic devices.

a Department of Mechanical Engineering, Boston University, Boston, MA, USA
b Photonics Center, Boston University, Boston, MA, USA
c Department of Biomedical Engineering, Boston University, Boston, MA, USA
d Division of Materials Science and Engineering, Boston University, Boston, MA, USA
† Department of Mechanical Engineering, Boston University, 110 Cummington Mall, Boston, MA 02215. E-mail: ekinci@bu.edu; Fax: +1-617-353-5866; Tel: +1-617-353-8670.
‡ Department of Biomedical Engineering, Boston University, 44 Cummington Mall, Boston, MA 02215. E-mail: jtien@bu.edu; Fax: +1-617-358-2835; Tel: +1-617-358-3055.

Since PDMS is elastic, the walls of the device distend under flow, albeit very slightly.[11–15] Our method employs interferometric microscopy to detect the extremely small (<0.4 μm) displacement of PDMS under typical fluid pressures, with a lateral resolution of ~ 9 μm. By ensuring that the displacement of the PDMS remains small so that the accompanying interstitial flow rate is small, this method of measuring IFP does not require large-scale movement of interstitial fluid, and we have attained a response time of ~ 5 min. We illustrate one possible application of the technique by using high-resolution IFP maps, in conjunction with computational modeling, to estimate the hydraulic properties of microscale engineered tissues.

Theory

In a PDMS fluidic device in which the pressure and displacement vary in two dimensions (x and y), we assume that the two fields are related linearly and locally:

$$P(x,y) = a(x,y)\zeta(x,y). \tag{1}$$

Here, $P(x,y)$ is the pressure exerted at the interface between the fluidic channel and the distensible PDMS surface, $\zeta(x,y)$ is the displacement of the outermost PDMS surface (*i.e.*, the surface in contact with air), and $a(x,y)$ is the local "stiffness" of the device. Eqn (1) can be regarded as an attempt to approximate a tube law in the limit of small displacements and small pressure gradients.[15,16]

If the distending PDMS device is filled with an adherent porous and elastic material, then the pressure $P(x,y)$ consists of separate stresses from interstitial fluid and from the porous solid skeleton.[17] In the case of soft tissues and gels, however, the solid pressure is negligible; for a strain of <1 μm/1 mm (as in the devices studied here) and a gel modulus on the order of 1 kPa, the solid stress is on the order of 1 Pa or less. These considerations imply that the local displacement of PDMS is proportional to the local fluid pressure in the gel, *i.e.*, IFP.

Knowing the stiffness a allows one to calculate IFP from a measured displacement map $\zeta(x,y)$. In a PDMS device, the local thickness of the microfluidic device may vary, so the stiffness may be a function of position but is assumed to be independent of displacement and pressure; that is, $a = a(x,y)$. Our proposed method to determine IFP is thus as follows: First, we measure the displacement of the device under uniform pressure(s) to obtain the local stiffness map $a(x,y)$. Second, we operate the device under conditions that subject the gel—and the tissue that it may contain—to pressure gradients, and use eqn (1) to obtain the pressure field. We validated the applicability of the proposed method with numerical simulations and applied it to experimental displacement data from cell-free gels and from microscale tissues.

Materials and methods

Cell culture

Mouse Lewis lung carcinoma cells (LLC; ATCC) and Madin-Darby canine kidney cells (MDCK; ATCC) were routinely cultured at 5% CO_2 in MEM (Invitrogen) that was supplemented with 10% calf serum (Invitrogen) and 1% glutamine–penicillin–streptomycin (Invitrogen). Bovine lung microvascular endothelial cells (BLMEC; VEC Technologies) were routinely cultured at 5% CO_2 on gelatin-coated dishes in MCDB131 (Caisson) that was supplemented with 10% fetal bovine serum (Atlanta Biologicals), 80 μM dibutyryl cyclic AMP (Sigma), 1 μg mL^{-1} hydrocortisone (Sigma), 25 μg mL^{-1} endothelial cell growth supplement (Biomedical Technologies), 2 U mL^{-1} heparin (Sigma), 0.2 mM ascorbic acid 2-phosphate (Sigma), and 1% glutamine–penicillin–streptomycin. All cells were used before passage ten.

Preparation of PDMS devices that contain collagen gels with and without cells

Fig. 1A and B show the basic fabrication steps and configurations of the microfluidic devices. Each device consisted of a patterned PDMS chamber that lay on top of a 25 mm × 75 mm glass slide to define a rectangular channel (1 mm wide, 1 mm high, 7 or 32 mm long) that was adjacent to 6 mm-diameter wells. The thickness of the PDMS that formed the "ceiling" of the channel varied between devices, and was in the range of 1 ± 0.3 mm. We introduced a solution of type I collagen (from rat tail, 7–8 mg mL^{-1}; BD Biosciences) into the channels, and we allowed it to gel at ~ 23 °C for thirty minutes. In some experiments, we molded the gel around one or two 120 μm-diameter needles (Seirin) that had been inserted into the channels; after gelation, we removed the needle(s) to yield a blind-ended cavity (the tip of which lay at the middle of the gel; Fig. 1A, bottom), a pair of opposing cavities (the tips of which were at the middle of the gel and slightly offset; Fig. 1B, middle), or an open cylindrical channel that spanned the gel (Fig. 1B, bottom), as described previously.[5,18,19] Gels were kept hydrated by adding phosphate-buffered saline (PBS) to each of the adjacent wells.

To form microscale tissues, we used 7 mm-long gels that contained a single blind-ended cavity (for LLC and MDCK cells) or an open channel (for BLMECs). For LLC and MDCK samples, we first conditioned the gels for at least one hour by adding the appropriate media to the wells. We then added a dense suspension of cells to the well that was adjacent to the open end of the cavity, and allowed interstitial flow of media to convect cells into the cavity. We seeded LLC cells until they formed a packed bed within the cavity, but limited the seeding time for MDCK cells so that only enough cells adhered to eventually organize into a confluent monolayer. We then washed the well with media to remove non-adherent cells, and added fresh media to both wells to promote interstitial flow and thereby provide nutrients to the cells within the cavity. For BLMEC samples, we first crosslinked gels with 20 mM genipin (Wako) for two hours, a step that was required to promote vascular adhesion and stability,[20] before conditioning with media and seeding cells. After seeding, flow was established in the BLMEC samples by interfacing the wells with reservoirs of media that was supplemented with 3% dextran (70 kDa; Sigma);[21,22] the reservoirs were held at pressures of ~ 800 Pa (8 cm H_2O) and 0 Pa, which yielded flow rates of 1–1.5 mL h^{-1}.
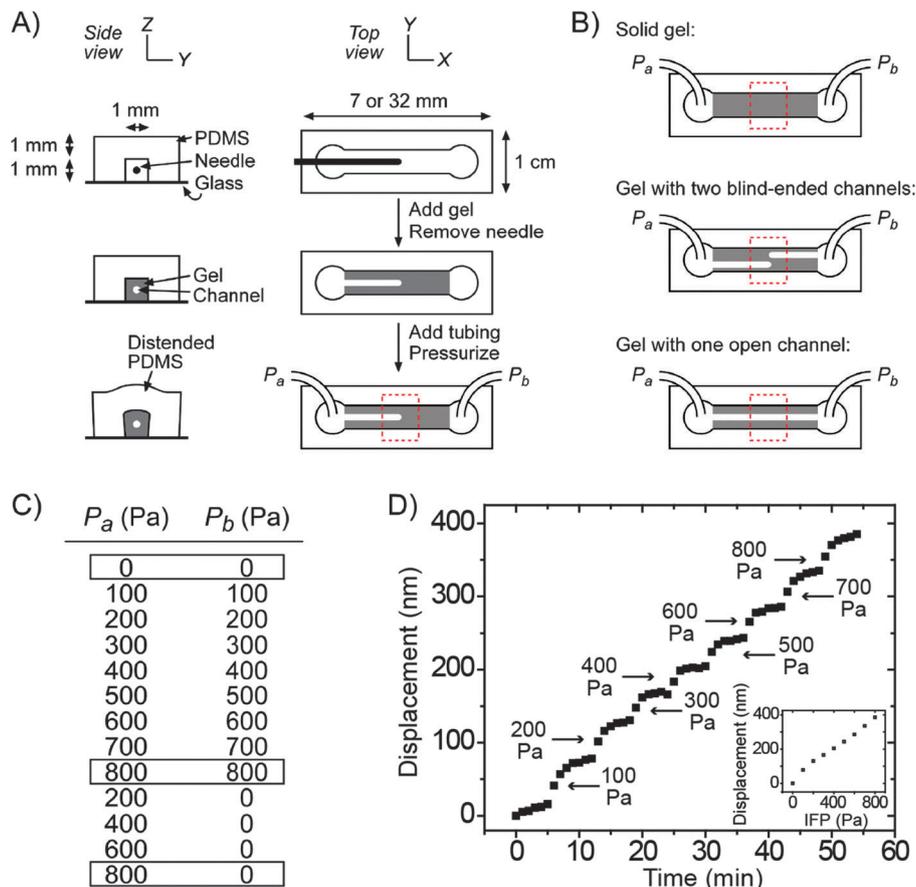
Fig. 1 Experimental design. (A) Schematic of the formation of a microfluidic PDMS device that contains a collagen gel with a blind-ended cavity. (B) Similar procedures generate devices that contain a solid gel, a gel with opposing blind-ended cavities, or a gel with an open channel. Red dashed rectangles refer to the imaging window. P_a and P_b are the pressures applied to the ends of the gel. (C) Sequence of applied pressures. For tissue-containing samples, we limited the pressure conditions to the three boxed ones. (D) Plot of outermost PDMS displacement *versus* time at a single point on a device that was filled with a solid collagen gel and subjected to a series of uniform hydrostatic pressures ($P_a = P_b = 0–800$ Pa, in steps of 100 Pa every six minutes). *Inset*, plot of displacement *versus* pressure.

Measurement and analysis of pressure-displacement data

One day after forming gels (for cell-free samples), one day after seeding (for LLC samples), or three days after seeding (for MDCK and BLMEC samples), we imaged the mechanical response of the devices. At these time points, the cells in the LLC, MDCK, and BLMEC samples had organized into a packed cell aggregate, a blind-ended epithelial tube, and an open endothelial microvessel, respectively. Scanning white light interferometry[23] was performed on a Zygo NewView 6300 microscope with a 2.5× Nikon interferometric infinite conjugate objective (NA = 0.075, WD = 10.3 mm). This microscope passes broadband light through an interferometric objective and splits it into two beams. One beam reflects from the sample surface, the other reflects from a flat reference surface, and both beams are then recombined and imaged on a CCD camera. White light has a short coherence length, so constructive interference occurs only when the path lengths of the two beams are nearly equal. For each pixel on the CCD, the modulation intensity of the interference signal is maximum when the two path lengths are exactly the same. Hence, scanning the

sample objective vertically and recording the modulation intensity allows one to construct a topographical map of the outermost surface.

To image a sample, we first interfaced its two wells with polyethylene tubing (Braintree Scientific) to reservoirs of saline and media for cell-free and cell-containing samples, respectively.[18] For cell-free samples, we kept the reservoirs at the same height, and raised and lowered them in tandem to generate uniform hydrostatic pressures of 0–800 Pa within the gel, in steps of 100 Pa. At each pressure, we measured the resulting height profile at the outermost surface of the PDMS in a rectangular region-of-interest (4.24 mm × 5.65 mm area, 480 × 640 CCD resolution) at the central section of the gel (red dotted rectangles in Fig. 1A and B). These measurements took place every minute; we typically recorded five consecutive measurements at a given pressure before changing the pressure. Next, we introduced a pressure difference across the ends of the gel by holding one end at 0 Pa and changing the pressure at the other end to 200–800 Pa in steps of 200 Pa. Again, we imaged the resulting deflection every minute for at least five minutes at each pressure condition. Each cell-free sample required up to

2 h to complete the entire sequence of pressure conditions, as listed in Fig. 1C.

For cell-containing samples, we minimized the imaging time, since the imaging was performed at room temperature. Thus, the pressure conditions consisted only of uniform 0 Pa, uniform 800 Pa, and a pressure difference of 800 Pa. Imaging these samples required only ~20 min each.

Surface profile data were analyzed with MATLAB R2010b ver. 7.11.0 (Mathworks). The height profile of the PDMS without any pressurization was subtracted from all data to yield two-dimensional displacement maps $\zeta(x,y)$ for the various pressure conditions. The stiffness map of the PDMS device was calculated by a linear fit of pressure *versus* displacement under uniform pressure conditions (for samples without cells) or from displacement data under 800 Pa uniform pressure only (for samples with cells). To calculate the two-dimensional pressure profiles in the case of pressure-driven flow, we multiplied the stiffness map by the measured displacement.

Numerical modeling

To validate the IFP profiles, we constructed finite-element models in COMSOL Multiphysics ver. 3.5a (Comsol) to solve for the pressure distribution within the gel and the elastic deformation of the PDMS device. Governing equations consisted of Darcy's Law for the gel and the constitutive equations of linear elastic solids for PDMS; only steady terms were retained. The two fields were coupled by assuming that the gel pressure (*i.e.*, IFP) acted as a load at the PDMS-gel interface. Since PDMS is nearly incompressible, we used models that treated pressure as an additional independent parameter in the calculation of the stress field within the PDMS.[24] The Young's modulus and Poisson's ratio of PDMS were set to 2.5 MPa and 0.4999, respectively. For small models [$<10^6$ degrees-of-freedom (DOF)], we solved the governing equations simultaneously; for large models (up to $\sim4 \times 10^6$ DOF), we solved Darcy's Law first and the elasticity equations second.

Adaptive meshing was used to resolve the stress concentration at the corners of the PDMS channel. Tests of mesh independence used two sequentially refined meshes that differed by at least two-fold in DOF; meshes were refined until these comparisons yielded a maximum pressure difference of <4 Pa at the PDMS-gel interface and a maximum displacement difference of <5 nm at the top surface of the PDMS (*i.e.*, the surface imaged in experiments).

For each gel configuration, we simulated an imaging experiment by cycling through the same sequence of pressure conditions as those used in experiments. For models that were designed to simulate LLC aggregates, we treated the blind-ended cavity as a porous medium of unknown permeability K_{LLC}, and set the ratio of K_{LLC} to the gel permeability K_{gel} to be 0.01–100. For models that were designed to simulate MDCK epithelium, we assumed the surface of the blind-ended cavity acted as a permeable membrane with hydraulic conductivity L_{MDCK}, and set L_{MDCK}/K_{gel} to be 0.01–100 cm^{-1}. For models that were designed to simulate BLMEC vessels, we assumed the surface of the open channel acted as a permeable membrane with hydraulic conductivity L_{BLMEC}, and set L_{BLMEC}/K_{gel} to be

0.01–100 cm^{-1}; at the downstream outlet, we set the fluid pressure in the well and gel to be equal, as justified previously.[25] For the BLMEC models, the pressure within the channel in the gel was found by solving the Navier–Stokes equations before determining the pressure within the gel itself.

Results and discussion

In a typical experiment, we subjected a gel-containing microfluidic device to a series of homogeneous pressures (Fig. 1C), and measured the resulting displacement fields at the outermost PDMS surface. These measurements showed that gel pressure (*i.e.*, IFP) and PDMS displacement were proportional, and thus yielded a two-dimensional stiffness map of the device. We then subjected the device to a pressure difference, thereby inducing two-dimensional IFP variations, and measured the displacement field. From the stiffness map, we calculated the heterogeneous pressure field at the PDMS-gel interface as the product of local stiffness and displacement.

Numerical validation

Since our proposed approach relies on an *ad hoc* assumption of linearity and local response (see Theory), we used detailed numerical models to validate the approach and to determine the accuracy of the IFP field that was calculated from PDMS displacement (Fig. 2). These models reflected three gel configurations that we examined experimentally: a solid gel (Fig. 2A), a gel with a single blind-ended cavity (Fig. 2B), and a gel with two opposing blind-ended cavities (Fig. 2C). Solving these models showed that, regardless of the exact gel configuration, the displacement of the PDMS was extremely modest; an 800 Pa uniform pressure within the gel led to less than ~400 nm displacement of the outermost PDMS surface. Moreover, the displacement was linearly proportional to the level of uniform pressure. We then solved for the displacement fields when the gels were subjected to a pressure difference (see Fig. 2 for the case of 800 Pa pressure difference). From these displacement fields, we deduced the IFP in the gel ["IFP (predicted)" in Fig. 2] by treating the computed displacements as if they were actual experimental datasets and using eqn (1).

These models also yielded the exact pressure fields within the gels ["IFP (computed)" in Fig. 2]. The predicted and exact IFP were virtually identical for the case of a solid gel and a gel with one cavity, with a maximum error of 0.3 and 4 Pa, respectively. For the case of a gel with opposing cavities, the maximum error was ~120 Pa, a larger value that we attribute to the steep pressure gradients (~100 Pa/0.1 mm) in the region between the tips of the cavities (Fig. 2C, bottom). These results suggest that our displacement-based method accurately predicts IFP when the pressure gradients are below ~1 kPa mm^{-1}.

Displacement and pressure fields in cell-free PDMS devices

Next, we applied the method to experimental displacement data from PDMS devices that contained a gel without cells. Since the gel is hydraulically resistive, it is possible that reaching a steady-state level of displacement would require a
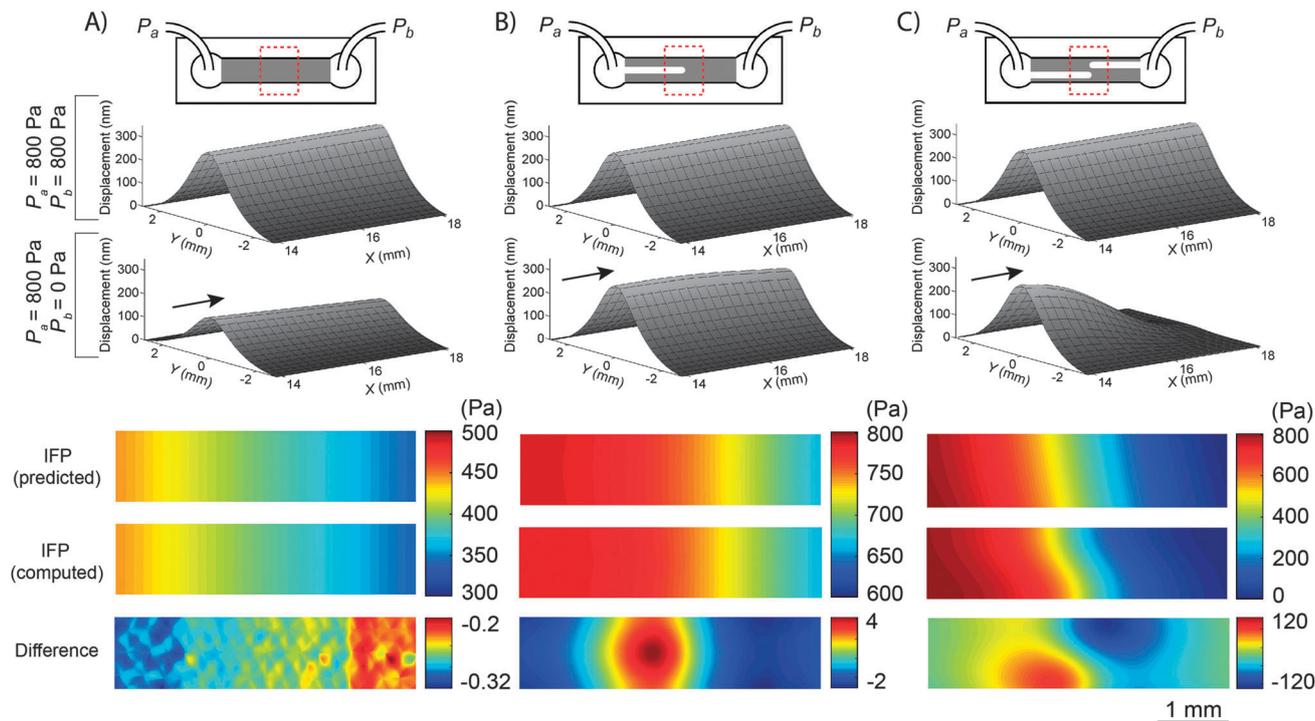
Fig. 2 Numerical validation of the method for calculating IFP from displacement maps. (A) Solid gel. (B) Gel with blind-ended cavity. (C) Gel with opposing cavities that were offset. In each panel, the upper and lower plots of displacement refer to the cases of $P_a = P_b = 800$ Pa, and $P_a = 800$ Pa and $P_b = 0$ Pa, respectively. Arrows point in the direction of lower pressure for the latter case. The upper, middle, and lower maps of IFP refer to the pressures predicted from the displacement maps, those computed directly from the models, and the difference between computed and predicted pressures, respectively.

measurable time lag after a sudden change in applied pressure. For this reason, we designed the dimensions of the PDMS chamber (in particular, the thickness of the wall above the gel) so that the displacement would be small. Given a maximum displacement of $\zeta \approx 400$ nm for an applied pressure of $P = 800$ Pa, a gel height and length of $H = 1$ mm and $L = 32$ mm, and a collagen gel hydraulic permeability of $K_{gel} \approx 5 \times 10^{-8}$ cm^4 dyn^{-1} s^{-1} (ref. 20), we estimated the interstitial flow speed to be on the order of $K_{gel}P/L \approx 1$ μm s^{-1}. Thus, the time required to transport interstitial fluid as the PDMS distends is on the order of $(\zeta L/H)/(1$ μm s$^{-1}) \approx 10$ s. Displacement *versus* time data showed that the displacement fields reached a steady-state within five minutes after changing the pressure condition (Fig. 1D). While using thinner PDMS would result in larger displacements at a given pressure (thus improving the sensitivity of the method), these displacements would require longer times to equilibrate. In our experience, a ∼1 mm-thick PDMS wall led to an acceptable balance of sensitivity and responsiveness.

Under uniform pressures, the measured displacements were proportional to applied pressure (Fig. 1D, inset), which provided a direct experimental validation of the assumptions underlying our approach and allowed us to calculate the stiffness map characteristic of each PDMS device. By definition, the stiffness is inversely proportional to the displacement under uniform pressure conditions; as expected, the stiffness was smallest over the channel centerline ($y = 0$ mm), where the displacement was largest (Fig. 3, plots with $P_a = P_b = 800$ Pa).

Measurement of the displacement fields under a pressure difference allowed us to calculate the IFP fields as a product of local stiffness and displacement for three gel configurations (solid gel, gel with a single blind-ended cavity, and gel with two opposing blind-ended cavities) using eqn (1).

Several features suggest that these calculated IFP fields accurately represent the actual pressure distributions at the PDMS-gel interface. Most importantly, the predicted sizes and directions of the IFP gradients matched those expected from the gel configuration. A pressure difference across a solid gel yielded a nearly linear IFP drop along the channel, with a value at the gel midpoint close to 400 Pa (*i.e.*, the average of the two applied pressures) (Fig. 3A). In a single blind-ended cavity, the pressure in the gel nearly matched the pressure applied to the open end of the cavity, as expected since the cavity provides a much smaller hydraulic resistance than the bulk gel (Fig. 3B). In opposing cavities, the pressure in the gel exhibited a much larger gradient, since the pressures applied to both open ends were easily transmitted to the central portion of the gel (Fig. 3C). Moreover, reversing the applied pressure difference led to a switch in the direction, but not the magnitude, of the predicted IFP gradients, as expected (Fig. 3B and C). We note that the predicted pressures in the gel with opposing cavities (200–600 Pa; Fig. 3C) had a narrower range than expected from numerical models (0–800 Pa; Fig. 2C); this difference may indicate an inherent inaccuracy when predicting IFP in gels with large pressure gradients.
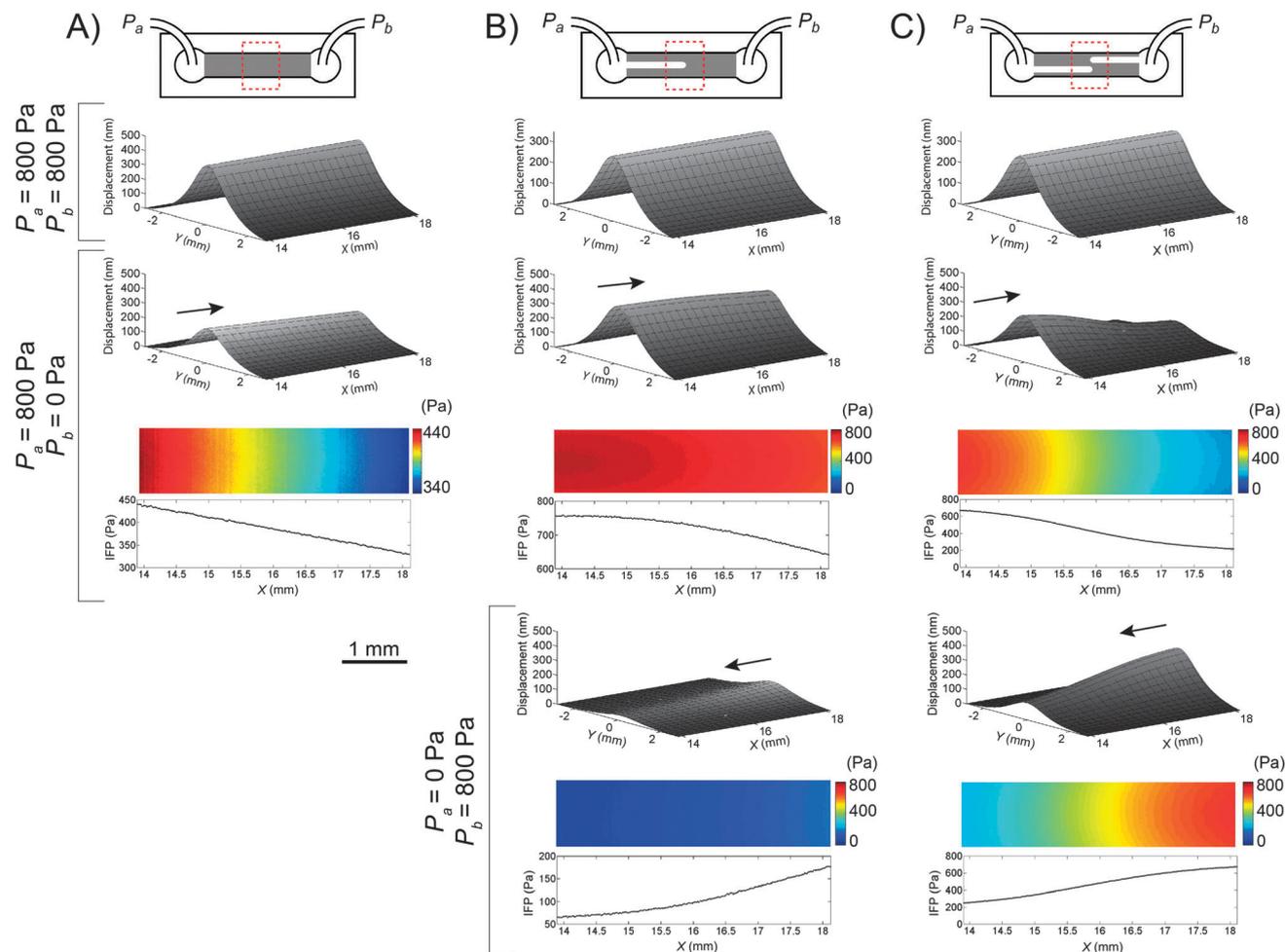
Fig. 3 Application of the method to obtain IFP maps in cell-free collagen gels. (A) Solid gel. (B) Gel with blind-ended cavity. (C) Gel with opposing cavities that were offset. In each panel, the upper plots of displacement refer to the case of $P_a = P_b = 800$ Pa. The remaining plots of displacement refer to $P_a = 800$ Pa and $P_b = 0$ Pa [(A)–(C), middle], and to $P_a = 0$ Pa and $P_b = 800$ Pa [(B) and (C), lower]. Arrows point in the direction of lower pressure for cases of non-uniform pressure. The IFP maps were calculated from the displacement maps, and plots of pressure *versus* axial distance along the PDMS centerline are shown.

Pressure fields in microscale tissues

To determine the suitability of this non-invasive technique to measure IFP in microscale tissues, we imaged the displacements of three distinct cell configurations: (1) a packed bed of LLC tumor cells in a blind-ended cavity in the gel (Fig. 4A), (2) a monolayer of MDCK epithelial cells that lined a blind-ended cavity (Fig. 4B), and (3) a microvessel of BLMECs that lined an open, perfused channel (Fig. 4C). Because the microscope stage that we used did not allow for sample heating, we limited the imaging to three pressure conditions (uniform 0 Pa, uniform 800 Pa, and a pressure difference of 800 Pa) to minimize cooling of the sample and cells. From the displacement field that was measured at 800 Pa uniform pressure, we calculated stiffness maps of the PDMS devices. As in the cell-free devices, each combination of stiffness map and displacement field yielded a predicted IFP field from eqn (1) when the tissue was placed under a pressure gradient.

We found the predicted IFP fields qualitatively matched what would be expected from the organization and type of cells within

each device. For the LLC sample (Fig. 4A), the IFP was intermediate between the two applied pressures, as expected for a packed bed. For the MDCK sample (Fig. 4B), IFP was very close to the low pressure applied at the end opposite to the opening of the channel; this result is expected since the epithelium should form an extremely tight hydraulic barrier, which would isolate the gel from the high pressure applied to the channel. For the BLMEC microvessel under flow (Fig. 4C), IFP was closer to the pressure applied at the downstream end; this result is consistent with the endothelium being a resistive barrier that is not as tight as epithelium, and is predicted in our previous work.[19,25]

To quantify these comparisons, we built computational models of these three cell-containing configurations and varied the hydraulic properties of the LLC packed bed and MDCK and BLMEC monolayers. The plots in Fig. 4 show the average (root-mean-square) difference between computationally obtained and experimentally predicted IFP maps as a function of cell hydraulic properties. With a gel hydraulic permeability of $\sim 5 \times 10^{-8}$ cm^4 dyn^{-1} s^{-1}, minimization of the differences between
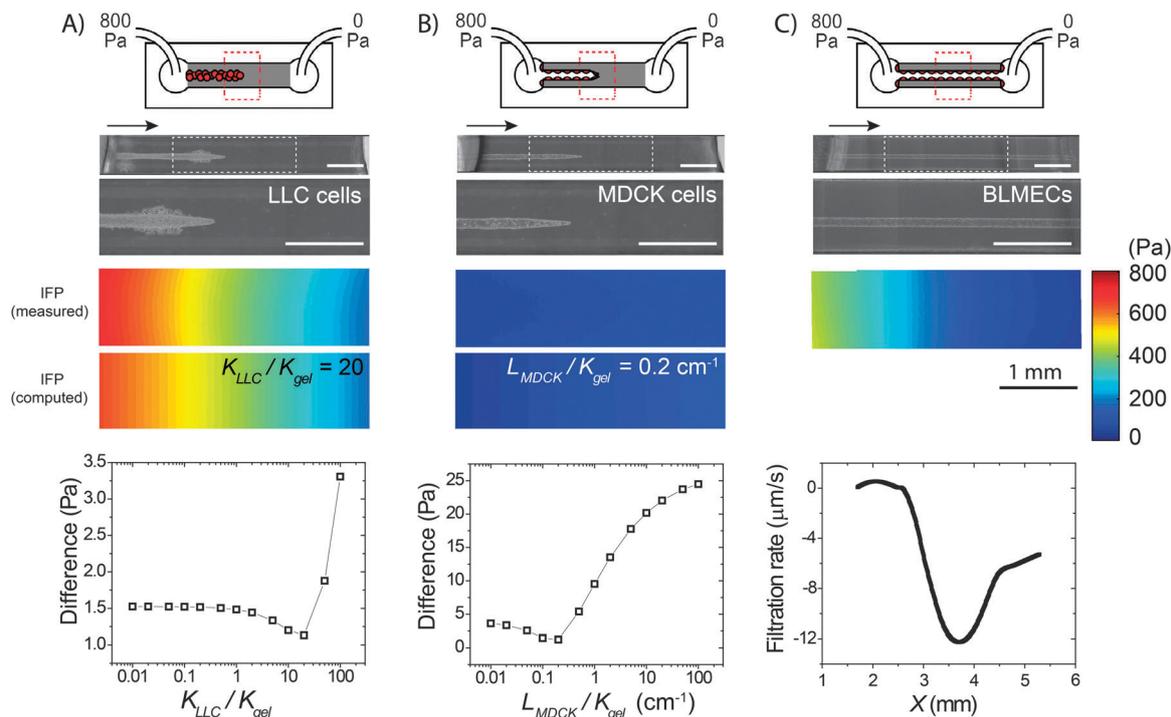
Fig. 4 Application of the method to obtain IFP maps in microscale tissues. (A) LLC aggregate within a blind-ended cavity. (B) MDCK epithelium that lined a blind-ended cavity. (C) BLMEC endothelium that lined an open, perfused channel. White dotted rectangles refer to the imaged area; scale bars refer to 1 mm. Arrows point in the direction of lower pressure. In (A) and (B), root-mean-square differences between the experimental IFP (upper maps) and those obtained from computational models with a range of cell hydraulic properties are plotted, and the numerically computed IFP maps using the optimal K_{LLC} or L_{MDCK} are shown (bottom maps). In (C), a plot of filtration rate *versus* axial distance along the vessel centerline is shown.

these models and the experimental data implied that the hydraulic permeability of the LLC packed bed was $\sim 10^{-6}$ cm^4 dyn^{-1} s^{-1} ($K_{\mathrm{LLC}}/K_{\mathrm{gel}} \approx 20$; Fig. 4A), and that the hydraulic conductivity of the MDCK monolayer was $\sim 10^{-8}$ cm^3 dyn^{-1} s^{-1} ($L_{\mathrm{MDCK}}/K_{\mathrm{gel}} \approx 0.2$ cm^{-1}; Fig. 4B). The estimated MDCK hydraulic conductivity agrees well with the reported value of 5×10^{-9} cm^3 dyn^{-1} s^{-1}.[26] Using the estimated LLC permeability and the Carman–Kozeny relation between permeability and porosity in packed beds,[27] we calculated that the porosity of the LLC aggregate is $\sim 49\%$, which agrees with the 40–50% range for random packing.[28] For LLC and MDCK tissues, using these estimates of hydraulic properties in computational models yielded computed IFP maps that matched closely with the experimental ones (Fig. 4, bottom maps).

For the BLMEC microvessel, computational models did not predict pressure fields that agreed well with experiment. This result suggests that the hydraulic properties of the endothelium were not uniform along the vessel wall, in contrast to the assumptions of the model. To better understand the filtration dynamics in the vessel, we used the IFP data to map the vascular filtration rate along the endothelium. Darcy's Law and conservation of fluid mass imply that

$$J(x) = -\frac{A}{2\pi R} K_{\mathrm{gel}} \frac{\partial^2 P}{\partial x^2}, \qquad (2)$$

where J is the filtration rate, A is the cross-sectional area of the gel, R is the vascular radius, and x is the distance along the

vessel axis. The calculated filtration rate was close to zero upstream, but became large and negative (indicating fluid reabsorption) downstream (Fig. 4C, bottom). This result is consistent with a non-uniform endothelial permeability and with the previous finding that endothelial detachment can occur downstream.[25]

Strictly speaking, the measured IFP maps are the pressures at the PDMS-gel interface, which may differ from the pressures experienced by cells. To determine the magnitudes of these pressure differences and their sensitivity to tissue geometry, we analyzed numerical models of LLC, MDCK, and BLMEC tissues in the 120 μm-diameter geometries used in experiments, as well as in narrower (60 μm-diameter) and wider (240 μm-diameter) configurations. We also modeled an MDCK epithelium within a T-shaped cavity, to represent a branched tissue. In all cases, the predicted IFP, IFP at the PDMS-gel interface, and IFP within the tissue proper matched closely, with a maximum relative difference of $<10\%$. Thus, the IFP maps can accurately represent pressures experienced by cells in the tissue.

Conclusions

To our knowledge, this study is the first to describe a non-invasive technique to measure interstitial fluid pressure within microscale tissues. The non-invasive nature of the method provides advantages in spatial and temporal resolution over

existing, invasive methods of measuring IFP. In the current work, the displacement reached a steady-state distribution within ∼5 min, which we could image instantaneously across an area of >20 mm^2 with ∼9 μm lateral resolution. The fine spatial resolution yielded a detailed two-dimensional IFP map that could be compared with those predicted by computational modeling to elucidate the hydraulic properties of tissues contained within the device. The method performed well when the IFP gradient was below ∼1 kPa mm^{-1}; using a thinner top PDMS wall should allow sharper gradients to be resolved, albeit at the cost of slower response. Microscope stage noise limits the accuracy of height measurements to ∼5 nm, corresponding to an intrinsic error in IFP of ∼10 Pa. Because displacements were steady-state values, time-dependent phenomena (e.g., visco-elastic relaxation) were not apparent; in principle, time-lapse measurements of displacement could yield information about the viscoelastic properties of the tissue, and we will investigate this possibility in a future study.

We emphasize that the method requires only that the microfluidic device that contains the tissue deform slightly under pressure, as is true for any PDMS-based device. No specialized elements need to be coupled with the microfluidics, and the device can thus operate in its native state. Moreover, the method measures the stiffness map of each device, so device-to-device variations in PDMS thickness or elastic modulus are automatically compensated for. These operating characteristics mean that we can routinely image samples and then return them to the incubator for further culture, without adding special modifications to the design of the tissue or PDMS device.

Studies of interstitial effects on tissue function have mostly focused on interstitial flow, rather than pressure, in part because non-invasive measurement of flow velocity is currently possible.[29] The ability to measure pressure along with flow velocity would enable direct calculation of the hydraulic permeability tensor of tissues and gels. Moreover, the ability to image IFP could yield deeper insights into the role of physical forces in tissue function. For instance, based on indirect evidence, we have proposed that stable adhesion of endothelium to a scaffold requires a vascular pressure that exceeds interstitial pressure by a critical amount.[30,31] Similarly, others have hypothesized that excessive IFP may retard the growth of tissues.[32,33] The current method would allow a direct test of these and related hypotheses.

By matching the experimental IFP data to computed pressure fields from numerical models, our method allows one to determine the hydraulic properties of the cultured cells. One can use these models to obtain an average hydraulic permeability (as for LLC aggregates and MDCK epithelium), or to locate spatial heterogeneities in cell permeability (as for BLMEC vessels). In principle, it should be possible to use the IFP data to map epithelial or endothelial permeability with similar spatial resolution (∼9 μm). Inverse modeling strategies[34,35] may provide analytical tools to translate IFP to permeability maps, which would enable new insights into how mechanical forces affect epithelial and endothelial permeability.

Acknowledgements

References

1 M. A. Swartz and M. E. Fleury, *Annu. Rev. Biomed. Eng.*, 2007, **9**, 229–256.
2 W. J. Polacheck, J. L. Charest and R. D. Kamm, *Proc. Natl. Acad. Sci. U. S. A.*, 2011, **108**, 11115–11120.
3 D. O. Miteva, J. M. Rutkowski, J. B. Dixon, W. Kilarski, J. D. Shields and M. A. Swartz, *Circ. Res.*, 2010, **106**, 920–931.
4 R. K. Jain, *Annu. Rev. Biomed. Eng.*, 1999, **1**, 241–263.
5 J. Tien, J. G. Truslow and C. M. Nelson, *PLoS One*, 2012, **7**, e45191.
6 J. W. Song and L. L. Munn, *Proc. Natl. Acad. Sci. U. S. A.*, 2011, **108**, 15342–15347.
7 P. A. Galie, D.-H. T. Nguyen, C. K. Choi, D. M. Cohen, P. A. Janmey and C. S. Chen, *Proc. Natl. Acad. Sci. U. S. A.*, 2014, **111**, 7968–7973.
8 M. Abkarian, M. Faivre and H. A. Stone, *Proc. Natl. Acad. Sci. U. S. A.*, 2006, **103**, 538–542.
9 N. Srivastava and M. A. Burns, *Lab Chip*, 2007, **7**, 633–637.
10 U. Ozerdem, *Microvasc. Res.*, 2009, **77**, 226–229.
11 T. Gervais, J. El-Ali, A. Günther and K. F. Jensen, *Lab Chip*, 2006, **6**, 500–507.
12 B. S. Hardy, K. Uechi, J. Zhen and H. Pirouz Kavehpour, *Lab Chip*, 2009, **9**, 935–938.
13 A. Orth, E. Schonbrun and K. B. Crozier, *Lab Chip*, 2011, **11**, 3810–3815.
14 W. Song and D. Psaltis, *Biomicrofluidics*, 2011, **5**, 044110.
15 O. Ozsun, V. Yakhot and K. L. Ekinci, *J. Fluid Mech.*, 2013, **734**, R1.
16 M. E. McClurken, I. Kececioglu, R. D. Kamm and A. H. Shapiro, *J. Fluid Mech.*, 1981, **109**, 391–415.
17 H. F. Wang, *Theory of Linear Poroelasticity With Applications to Geomechanics and Hydrogeology*, Princeton University Press, Princeton, NJ, 2000, p. 287.
18 G. M. Price and J. Tien, in *Microdevices in Biology and Engineering*, ed. S. N. Bhatia and Y. Nahmias, Artech House, Boston, MA, 2009, pp. 235–248.
19 K. H. K. Wong, J. G. Truslow, A. H. Khankhel, K. L. S. Chan and J. Tien, *J. Biomed. Mater. Res., Part A*, 2013, **101**, 2181–2190.
20 K. L. S. Chan, A. H. Khankhel, R. L. Thompson, B. J. Coisman, K. H. K. Wong, J. G. Truslow and J. Tien, *J. Biomed. Mater. Res., Part A*, 2014, **102**, 3186–3195.
21 K. M. Chrobak, D. R. Potter and J. Tien, *Microvasc. Res.*, 2006, **71**, 185–196.
22 A. D. Leung, K. H. K. Wong and J. Tien, *J. Biomed. Mater. Res., Part A*, 2012, **100**, 1815–1822.
23 L. Deck and P. de Groot, *Appl. Opt.*, 1994, **33**, 7334–7338.

24 G. A. Holzapfel, *Nonlinear Solid Mechanics*, Springer-Verlag, New York, NY, 2000, p. 455.

25 G. M. Price, K. H. K. Wong, J. G. Truslow, A. D. Leung, C. Acharya and J. Tien, *Biomaterials*, 2010, **31**, 6182–6189.

26 M. R. Turner, *Exp. Physiol.*, 1992, **77**, 321–329.

27 J. Bear, *Dynamics of Fluids in Porous Media*, Dover Publications, New York, NY, 1988.

28 G. Y. Onoda and E. G. Liniger, *Phys. Rev. Lett.*, 1990, **64**, 2727–2730.

29 S. R. Chary and R. K. Jain, *Proc. Natl. Acad. Sci. U. S. A.*, 1989, **86**, 5385–5389.

30 K. H. K. Wong, J. G. Truslow, A. H. Khankhel and J. Tien, in *Vascularization: Regenerative Medicine and Tissue Engineering*, ed. E. M. Brey, CRC Press, Boca Raton, FL, 2014, pp. 109–124.

31 J. Tien, *Curr. Opin. Chem. Eng.*, 2014, **3**, 36–41.

32 C. M. Nelson and J. P. Gleghorn, *Annu. Rev. Biomed. Eng.*, 2012, **14**, 129–154.

33 J. W. DiFiore, D. O. Fauza, R. Slavin, C. A. Peters, J. C. Fackler and J. M. Wilson, *J. Pediatr. Surg.*, 1994, **29**, 248–257.

34 R. C. Aster, B. Borchers and C. H. Thurber, *Parameter Estimation and Inverse Problems*, Academic Press, Oxford, UK, 7 edn, 2013, p. 360.

35 P. C. Hansen, *Discrete Inverse Problems*, SIAM, Philadelphia, PA, 7 edn, 2010, p. 213.